AFRL-ML-WP-TR-2006-4169

SIMULATING MACROSEGREGATION IN VAR INGOTS OF TITANIUM ALLOY DURING SOLIDIFICATION

D.R. Poirier
P.K. Sung

The University of Arizona
Department of Materials Science and Engineering
Tucson, AZ 85721-0012

JUNE 2006

Final Report for 15 May 2002 – 31 March 2006

STINFO COPY

MATERIALS AND MANUFACTURING DIRECTORATE
AIR FORCE RESEARCH LABORATORY
AIR FORCE MATERIEL COMMAND
WRIGHT-PATTERSON AIR FORCE BASE, OH 45433-7750

NOTICE

Using Government drawings, specifications, or other data included in this document for any purpose other than Government procurement does not in any way obligate the U.S. Government. The fact that the Government formulated or supplied the drawings, specifications, or other data does not license the holder or any other person or corporation; or convey any rights or permission to manufacture, use, or sell any patented invention that may relate to them.

This report was cleared for public release by the Air Force Research Laboratory Wright Site (AFRL/WS) Public Affairs Office (PAO) and is releasable to the National Technical Information Service (NTIS). It will be available to the general public, including foreign nationals.

PAO Case Number: AFRL/WS 06-1622, 27 June 2006.

THIS TECHNICAL REPORT IS APPROVED FOR PUBLICATION.

//Signature//   //Signature//
_____   _____
S. LEE SEMIATIN, Project Engineer   ROLLIE DUTTON, Branch Chief
Metals Branch   Metals Branch
Metals, Ceramics & NDE Division   Metals, Ceramics & NDE Division

//Signature//
_____
GERALD J. PETRAK, Assistant Division Chief
Metals, Ceramics & NDE Division
Materials & Manufacturing Directorate

This report is published in the interest of scientific and technical information exchange and its publication does not constitute the Government's approval or disapproval of its ideas or findings.

REPORT DOCUMENTATION PAGE			*Form Approved* *OMB No. 0704-0188*

The public reporting burden for this collection of information is estimated to average 1 hour per response, including the time for reviewing instructions, searching existing data sources, searching existing data sources, gathering and maintaining the data needed, and completing and reviewing the collection of information. Send comments regarding this burden estimate or any other aspect of this collection of information, including suggestions for reducing this burden, to Department of Defense, Washington Headquarters Services, Directorate for Information Operations and Reports (0704-0188), 1215 Jefferson Davis Highway, Suite 1204, Arlington, VA 22202-4302. Respondents should be aware that notwithstanding any other provision of law, no person shall be subject to any penalty for failing to comply with a collection of information if it does not display a currently valid OMB control number. **PLEASE DO NOT RETURN YOUR FORM TO THE ABOVE ADDRESS**.

1. REPORT DATE *(DD-MM-YY)* June 2006	2. REPORT TYPE Final	3. DATES COVERED *(From - To)* 05/15/2002 – 03/31/2006	
4. TITLE AND SUBTITLE SIMULATING MACROSEGREGATION IN VAR INGOTS OF TITANIUM ALLOY DURING SOLIDIFICATION		5a. CONTRACT NUMBER F33615-02-1-5219	
		5b. GRANT NUMBER	
		5c. PROGRAM ELEMENT NUMBER 61102F	
6. AUTHOR(S) D.R. Poirier P.K. Sung		5d. PROJECT NUMBER 4347	
		5e. TASK NUMBER 21	
		5f. WORK UNIT NUMBER 05	
7. PERFORMING ORGANIZATION NAME(S) AND ADDRESS(ES) The University of Arizona Department of Materials Science and Engineering Tucson, AZ 85721-0012		8. PERFORMING ORGANIZATION REPORT NUMBER	
9. SPONSORING/MONITORING AGENCY NAME(S) AND ADDRESS(ES) Materials and Manufacturing Directorate Air Force Research Laboratory Air Force Materiel Command Wright-Patterson AFB, OH 45433-7750		10. SPONSORING/MONITORING AGENCY ACRONYM(S) AFRL-ML-WP	
		11. SPONSORING/MONITORING AGENCY REPORT NUMBER(S) AFRL-ML-WP-TR-2006-4169	

12. DISTRIBUTION/AVAILABILITY STATEMENT
Approved for public release; distribution is unlimited.

14. ABSTRACT (*Maximum 200 words*)
Simulations of VAR-ingots of Ti-6A1-4V, with emphasis on predicting macrosegregation of oxygen, are presented. MULTIA simulations showed that segregation patterns in the ingots result largely from the strong convection in the melt pool. Permeabilities in the mushy zones were less important. Simulations revealed more details in the macrosegregation patterns when the element-size selected for the calculation was reduced to 7.2 mm x 10.8 mm. the extent of the segregation, as the difference between the maximum (≈0.22 wt.%) and minimum (≈0.15 wt.%) concentrations of oxygen were about the same for both element sizes. A band of negative segregation near and running parallel to the ingot-surface was simulated, but the finer sized elements revealed a more intense band. Since primary arm spacings in titanium alloys are not available, primary dendrite arm spacings in Ti-6A1-4V were estimated. A summary-status of the use of software by VAR titanium-ingot producers in the USA is also given. In its initial stages, the research was on "Formation of Microporosity in Nickel-Base Thin Wall Casings," so a brief summary of microporosity in experimental castings is presented.

15. SUBJECT TERMS
macrosegregation, simulation, VAR ingots titanium alloy, solidification

16. SECURITY CLASSIFICATION OF:			17. LIMITATION OF ABSTRACT: SAR	18. NUMBER OF PAGES 50	19a. NAME OF RESPONSIBLE PERSON (Monitor) Dr. S. Lee Semiatin
a. REPORT Unclassified	b. ABSTRACT Unclassified	c. THIS PAGE Unclassified			19b. TELEPHONE NUMBER *(Include Area Code)* N/A

Standard Form 298 (Rev. 8-98)
Prescribed by ANSI Std. Z39-18

TABLE OF CONTENTS

LIST OF FIGURES

Summary

      Simulations of VAR-ingots of Ti-6Al-4V, with emphasis on predicting macrosegregation of oxygen, are presented. Processing conditions for the simulations were selected in with RMI Titanium of Niles, Ohio, who provided the output from their software (BAR), which was used to assist in analyzing an experimental ingot. BAR does not capture macrosegregation, so its calculated Lorentz forces were extracted and included as body forces along with the gravity body forces in MULTIA. MULTIA simulations showed that segregation patterns in the ingots result largely from the strong convection in the melt pool. Permeabilities in the mushy zones were less important. Simulations revealed more details in the macrosegregation patterns when the element-size selected for the calculation was reduced to 7.2 mm x 10.8 mm. The extent of the segregation, as the difference between the maximum (≈ 0.22 wt.%) and minimum (≈ 0.15 wt.%) concentrations of oxygen were about the same for both element sizes. A band of negative segregation near and running parallel to the ingot-surface was simulated, but the finer sized elements revealed a more intense band. Another feature was a broad vertical band of positive segregation, which originated at the center-bottom and migrated to the half-width position, where it persisted to about 5/8 of the ingot length. Since primary arm spacings in titanium alloys are not available, primary dendrite arm spacings in Ti-6Al-4V were estimated. A summary-status of the use of software by VAR titanium-ingot producers in the USA is also given. In its initial stages, the research was on "Formation of Microporosity in Nickel-Base Thin Wall Castings," so a brief summary of microporosity in experimental castings is presented (Appendix C).

I. Introduction

      In order to simulate macrosegregation in VAR ingots, an "in-house" code, MULTIA, was used. It is based on a complete model of transport phenomena (energy equation, conservation equations for each solute, momentum equation, and continuity). The mushy zone is treated as a porous medium in which the permeability varies with fraction solid. Mathematical details underlying MULTIA are in Appendix A. Convection in the melt pool is driven by both buoyancy and Lorentz forces. The latter are particularly important in Ti-ingot processing. Selection of the processing conditions for the simulations was done with RMI Titanium of Niles, Ohio, who provided the output from a proprietary code, BAR. BAR simulates convection in the melt pool and demarcates the mushy zone. A first-order turbulence model with Lorentz forces is included, but BAR is not set up to capture macrosegregation. In this work, Lorentz forces were extracted from BAR and included as body forces in MULTIA so that the interaction between the melt pool and the mushy zone were simulated. Equilibrium partition ratios of alloy elements were provided by the Air Force Materials Laboratory (AFML).

      In this report, simulations of the macrosegregation in VAR-ingots of Ti-6Al-4V are reported. The output comprises: the temperature field and the position of the mushy-zone; the concentrations of Al, V, O and Fe and their variations across the diameter of the ingot; and velocities in the melt pool and the mushy zone. Subsidiary information includes the Lorentz forces in the melt pool, the volume fraction of solid throughout the mushy-zone, and microsegregation characteristics.

II. Estimating Dendrite Spacings in Ti-6Al-4V

A. *Connection between Permeability and Dendritic Structure.*

Since permeability has units of m^2, a length scale of the dendritic structure must be assigned to estimate the permeability and hence the strength of convection during solidification of alloys. We devise relationships for estimating the dendritic spacings in Ti-6Al-4V alloy for the purpose of simulating the formation of macrosegregation in ingots of the subject alloy. The convection in the mushy zone is modeled with a momentum equation, which includes inertial and viscous terms along with the Darcy term [1], in which the permeability tensor appears. Permeability ($\mathbf{K}$) has dimensions of length-squared. For columnar-dendritic growth [2]:

$$\mathbf{K} = d_1^{\,2}\, f_1(g_L) \tag{1}$$

where $f_1(g_L)$ is a function of the volume fraction of the interdendritic liquid and d_1 is the primary dendrite-arm spacing. Dendrite spacings are reported for aluminum alloys, ferrous alloys and Ni-base alloys [4, 5], but relatively few data on titanium alloys exist. Nurminen and Brody [6] measured and reported secondary arm spacings (d_2, μm) in several binary alloys, including Ti-Al and Ti-V. Data for primary arm spacings, however, are not available. Here the secondary arm spacings for Ti-Al and Ti-V alloys are summarized, from which primary arm spacings are estimated.

B. *Secondary Dendrite Arm Spacings*

Nurminen and Brody [6] measured and correlated secondary dendrite arm spacings with solidification time (θ, s) as

$$d_2 = C\, \theta^n \tag{2}$$

where d_2 is the secondary spacing (μm) and C and n are constants. The constants for the Ti-V and for the Ti-Al alloys are about the same, so each was treated as one data set. C is

$$C = 184.36 - 41.453\, x + 4.2375\, x^2 - 0.1577\, x^3 \tag{3}$$

where x is either wt.% Al or wt.% V. Ripening theory applied to secondary dendrite arm spacing predicts n of 1/3 [4]. The values found range from 0.312 to 0.444, in rough agreement with the theoretical value. As a function of concentration,

$$n = 0.3411 + 0.0053\, x \tag{4}$$

Since the binaries have similar constants, Eqs. (3) and (4) were utilized by taking x as the sum of the concentrations of Al and Ti in the commercial alloy, Ti-6Al-4V. For the Ti64 alloy, we use a composition (in wt.%) of Ti - 5.72 Al - 4.10 V - 0.22 Fe - 0.183 O; hence $C = 36.585$ and $n = 0.3931$ from Eqs. (3) and (4), respectively.

In a rapidly solidified Ti-alloy (Ti-15V-3Al-5Sn-3Cr), a relationship between the secondary dendrite arm spacing and cooling rate is presented [7]. This relationship, however,

is based on applying a heat transfer model for a rapid solidification scenario; the empirical results of Nurminen and Brody [6] are deemed more reliable, especially for cooling rates encountered in ingots and castings.

C. *Primary Dendrite Arm Spacings*

In order to estimate primary dendrite arm spacing in Ti64, the data collected by Whitesell [5] for both primary and secondary dendrite arm spacings in Ni-base superalloys were consulted. In terms of a cooling rate, the dendrite arm spacings are approximated by

$$d_1 \ = \ 160 \, \varepsilon_t^{-0.421} \tag{5}$$

and

$$d_2 \ = \ 160 \, \varepsilon_t^{-0.391} \tag{6}$$

The cooling rate is in K/s, and the arm spacings are in μm. The cooling rate in Eqs. (5) and (6) are $\varepsilon_t = GR$, where G and R are the thermal gradient (K/cm) and solidification rate (cm/s) measured in the liquid at the dendrite tips. Since this G differs from that through the mushy zone, then ε_t differs from the usual cooling rate based on solidification time, namely:

$$\varepsilon \ = \ \frac{T_L \ - \ T_E}{\theta} \tag{7}$$

where T_L is the liquidus and T_E is the non-equilibrium solidus.

A relationship between ε_t and ε was sought by making use of empirical cooling curves in a Ti-alloy casting given by Nurminen and Brody [6] and cooling curves for Fe - 26 wt.% Ni given by Flemings et al. [8]. The ferrous alloy has a liquidus lower than that of the Ti64 alloy (1653 °C), but it is similar to the Ti64 alloy in that it has a relatively small solidification temperature range. In all eight sets of cooling rates were regressed, resulting in

$$\varepsilon \ = \ 6.614 \, \varepsilon_t \tag{8}$$

The cooling rates covered by Eq. (8) are up to 5.3 K/s for ε and 0.75 K/s for ε_t.
To convert from cooling rate to solidification time, solidification temperatures of the Ti64 alloy of the composition Ti-5.72 Al-4.10 V-0.22 Fe-0.183 O were used. The liquidus is 1926 K. The temperature at the end of solidification must lie between the equilibrium solidus (1964.5 K) and the non-equilibrium solidus assuming no diffusion in the solid during solidification (1881.4 K). Using Eq. (2) with the constants for the Ti64 alloy, solidification times were varied from 1 to 100 s, and two cooling rates in the mushy zone were calculated for each solidification time. For one cooling rate it was assumed that T_E was 1964.5 K, and for the other it was 1881.4 K. Then the cooling rates were used to deduce the primary dendrite arm spacings by the ratio given by combining Eqs. (5) and (6):

$$\frac{d_1}{d_2} = 4.893\,\varepsilon_t^{-0.03} \tag{9}$$

Finally the dendritic spacings were put in terms of ε, which is the usual cooling rate given by Eq. (7).

Dendrite spacings calculated by the above procedures are shown in Fig. 1. The secondary dendrite arm spacing is the same as Eq. (2) with $C = 36.585$ and $n = 0.3931$. There are two lines (practically superimposed) for the primary dendrite arm spacing, depending on the selection of the temperature for the solidus. The average of the two lines is

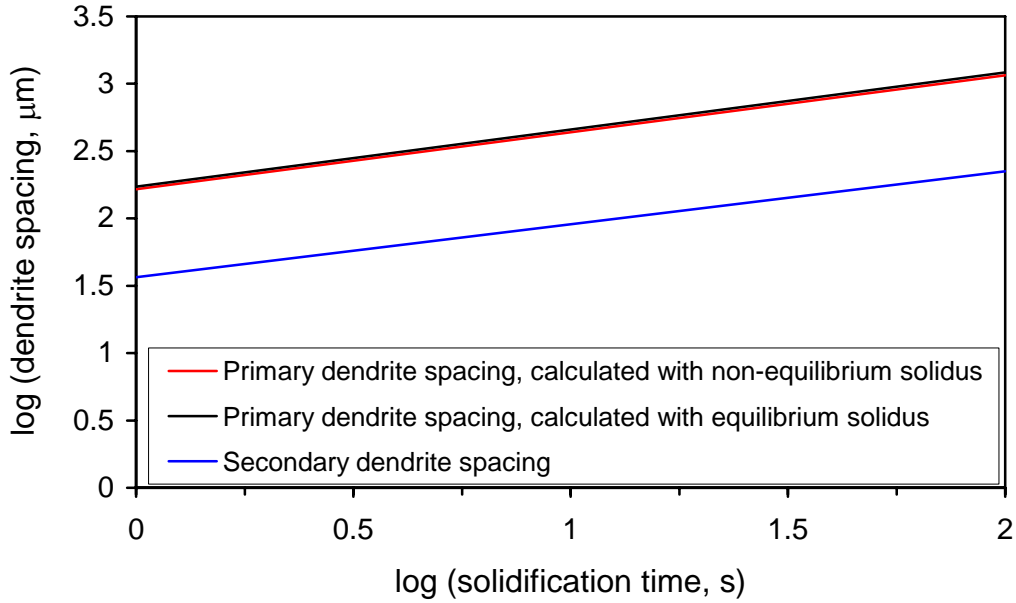$$d_1 = 168.62\,\varepsilon^{-0.4231} \tag{10}$$

Fig. 1. Calculated primary and secondary arm spacings in Ti-6Al-4V.

III. Macrosegregation Simulations

A. *Role of Primary Dendrite Arm Spacing on Macrosegregation*

Simulations of solidification of an ingot of Ti-6Al-4V with a melting condition provided by RMI Titanium Company (Proposed Case 11). Two ingots are simulated; one is simulated assuming a primary arm spacing of 800 μm and the other with a primary arm spacing of 300 μm. By studying these dendritic length scales, the role of permeability on the overall macrosegregation was ascertained. It is shown below, that with the larger dendrite arm spacing, the simulated macrosegregation is somewhat stronger, but the difference is not as great as expected if flow throughout the mushy zone was important. Therefore, most of the macrosegregation is the result of the interacting flows between the liquid pool and the leading part of the mushy zone.

B. *MULTIA Simulation of the VAR-Ingot*

In VAR-processing, the Lorentz force, the gravity force (*i.e.*, buoyancy force) and the solidification shrinkage drive the convection. The pool flow of the VAR ingot is caused by a competition between the Lorentz force and buoyancy force. The buoyancy force is dominant for low-current VAR-ingots (*e.g.*, Ni-base superalloys [9]), whereas the Lorenz force is dominant for the high-current VAR ingot (*e.g.*, Ti-base alloys).

The MULTIA model incorporates solidification theory, mainly to account for the partitioning of each alloy element between solid and liquid. The density of the liquid in the mushy zone or in the all-liquid zone depends on its constitution and temperature; hence the liquid density varies spatially and temporally and is subject to gravity-driven convection [10-13].

The program starts with a mesh that has four layers of elements in the vertical direction. As mass enters the liquid pool from the electrode, new layers of elements are added at the top of the ingot. The addition of layers stops when the maximum height specified is reached. The dimension of the fully-grown domain is 43 cm in width and 165 cm in height.[**] There are 30 elements across the width and 76 elements along the height of the complete ingot, and each element in the MULTIA-mesh is 14.3 mm × 21.7 mm.

As presently structured, MULTIA is not furnished to calculate the thermal boundary conditions and electromagnetic forces in the VAR process. Therefore, to effect a MULTIA-simulation, the thermal boundary conditions and the electromagnetic body-forces (Lorentz forces) were taken from the BAR-output. For convenience and to avoid interpolations, the mesh of the MULTIA simulation is constructed to be identical to that of the BAR simulation. From the BAR results, the heat transfer coefficients on each boundary were obtained and applied as thermal boundary conditions for a MULTIA simulation. At the boundary nodes along the left side (line of symmetry), no thermal flux is employed. The MULTIA simulation starts with an all-liquid alloy of the nominal composition at a uniform temperature of 1950 K (17 K higher than the liquidus) in the bottom four layers of elements.

Figure 2 shows the results from the MULTIA simulation and illustrate the

---

[**] Cartesian coordinates are used for the results reported here. Axi-symmetric coordinates can be used, but the computer runs are longer than when Cartesian coordinates are used.

calculated velocities in the liquid pool. These figures represent output after 6000 s and 8700 s of solidification of the ingot. They show convection patterns, which are qualitatively similar to the BAR result. The maximum velocity in the MULTIA-result (~40 cm/s) is greater than that in the BAR-result (~17 cm/s). In MULTIA the viscosity of the liquid equals the "molecular" viscosity, whereas BAR employs an "eddy" viscosity to account for turbulence.

Figures 3(a) and 3(b) show the resulting macrosegregation of oxygen after 8700 s of solidification of the ingot. Figure 3(a) is the result simulated with a large primary arm spacing of 800 μm for the permeability in mush zone, and Fig. 3(b) is with a small primary dendrite arm spacing of 300 μm. Notice that there is a band of positive segregation of oxygen near and at the mid-width of the ingot for the both cases. The simulation with the larger primary spacing enhances segregation. The O-concentrated region in the upper area near the wall is reduced in the case with the smaller arm spacing. For the larger spacing (800 μm), the maximum concentration of oxygen is 0.334 wt.%, which is 83 % higher than its nominal composition (0.183 wt.% O). For the smaller primary arm spacing (300 μm), the maximum concentration of oxygen is 0.280 wt.%, which is 53 % higher than its nominal composition.

Near the right side of each simulated ingot, there is a vertical band depleted in oxygen. Oxygen has a partition ratio greater than one, whereas iron has a partition ratio less than one. The bands, therefore, are enriched in iron and depleted in oxygen; the bands appeared to be weak freckles. As discussed in the next section, however, the freckling-mechanism, in which less dense liquid in the upper part of the mushy zone near the dendrite tips flows vertically upward and exits into the liquid pool, was discounted.

C. *Sensitivity of Calculations on Mesh Spacing*

The sensitivity of finite element mesh spacing on MULTIA-simulations of macrosegregation was studied. A systematic sensitivity analysis of mesh spacing on simulating macrosegregation during directional solidification (DS) [14] was consulted. The recommended elements should be no larger than $2\,d_1$ in the horizontal direction and $1.5\,D/V$ in the vertical direction), where d_1 is the primary arm spacing, D is the diffusivity in the liquid, and V is the growth rate. A sensitivity analysis of mesh spacing was applied to a DS domain of Ti-6Al-4V alloy with goal of finding an optimum mesh that could be applied to simulations of VAR-ingots. No freckles, however, were found in the Ti-6Al-4V alloy, and in this DS-scenario the alloy segregated very little. Hence, this set of DS-simulations did not conclusively indicate an optimum mesh.

To see the effect of the mesh spacing on simulated macrosegregation in VAR-ingots, a refined mesh spacing was employed. The dimension of the fully-grown domain is 43 cm in width and 165 cm in height. For the simulations of Figs. 4-6, there were 30 elements across the width and 76 elements along the height of the complete ingot, so each element in the mesh was 14.3 mm × 21.7 mm. In this section, the mesh is 60 elements across the width and 152 elements along the height, so each element in the mesh is 7.2 mm × 10.8 mm.

Fig. 2: Velocities calculated from MULTIA: (a) after 6000 s and (b) after 8700 s. The extent of the mushy zone is also shown. Dimensions are in m.
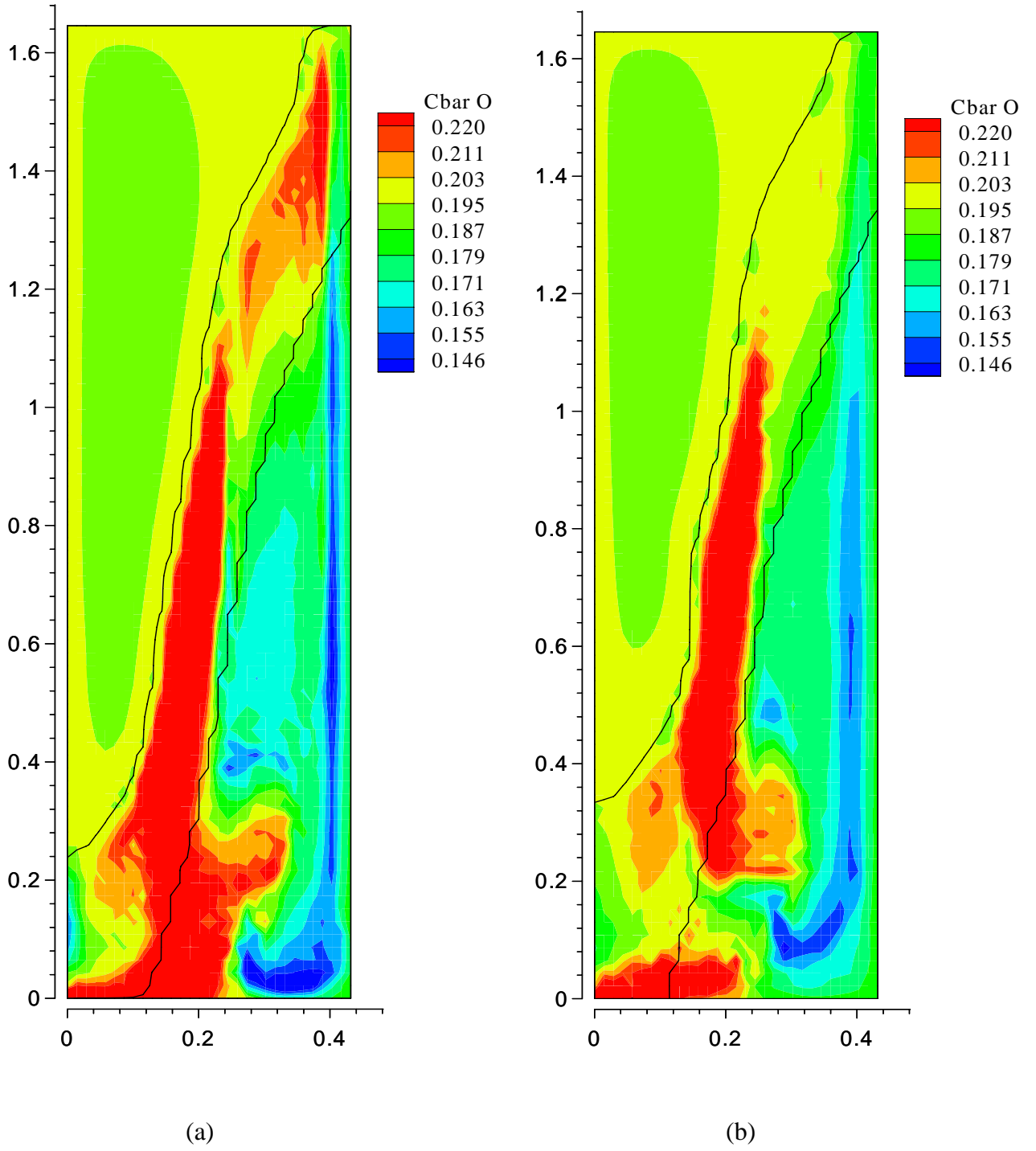
Fig. 3: Macrosegregation of oxygen calculated from MULTIA after 8700 s of ingot solidification: (a) primary arm spacing is 800 μm and (b) primary arm spacing is 300 μm. The extent of the mushy zone is also shown. Dimensions are in m.
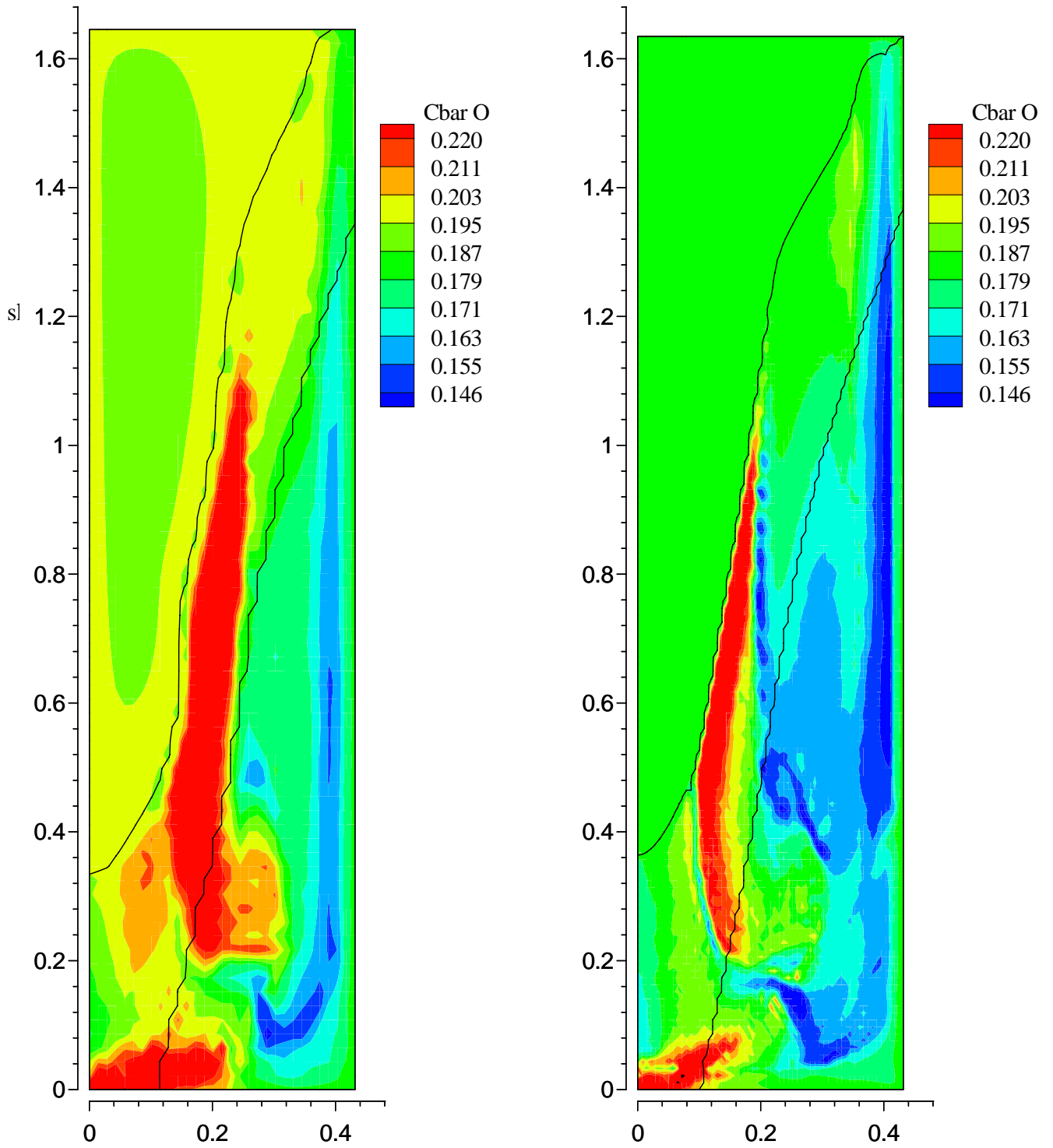
Fig. 4: Macrosegregation of oxygen calculated from MULTIA after 8700 s of ingot solidification with a primary arm spacing of 300 μm: (a) element size in mesh is 14.3 mm x 21.7 mm and (b) 7.2 mm x 10.8 mm. The extent of the mushy zone is also shown. DImensions are in m.

9
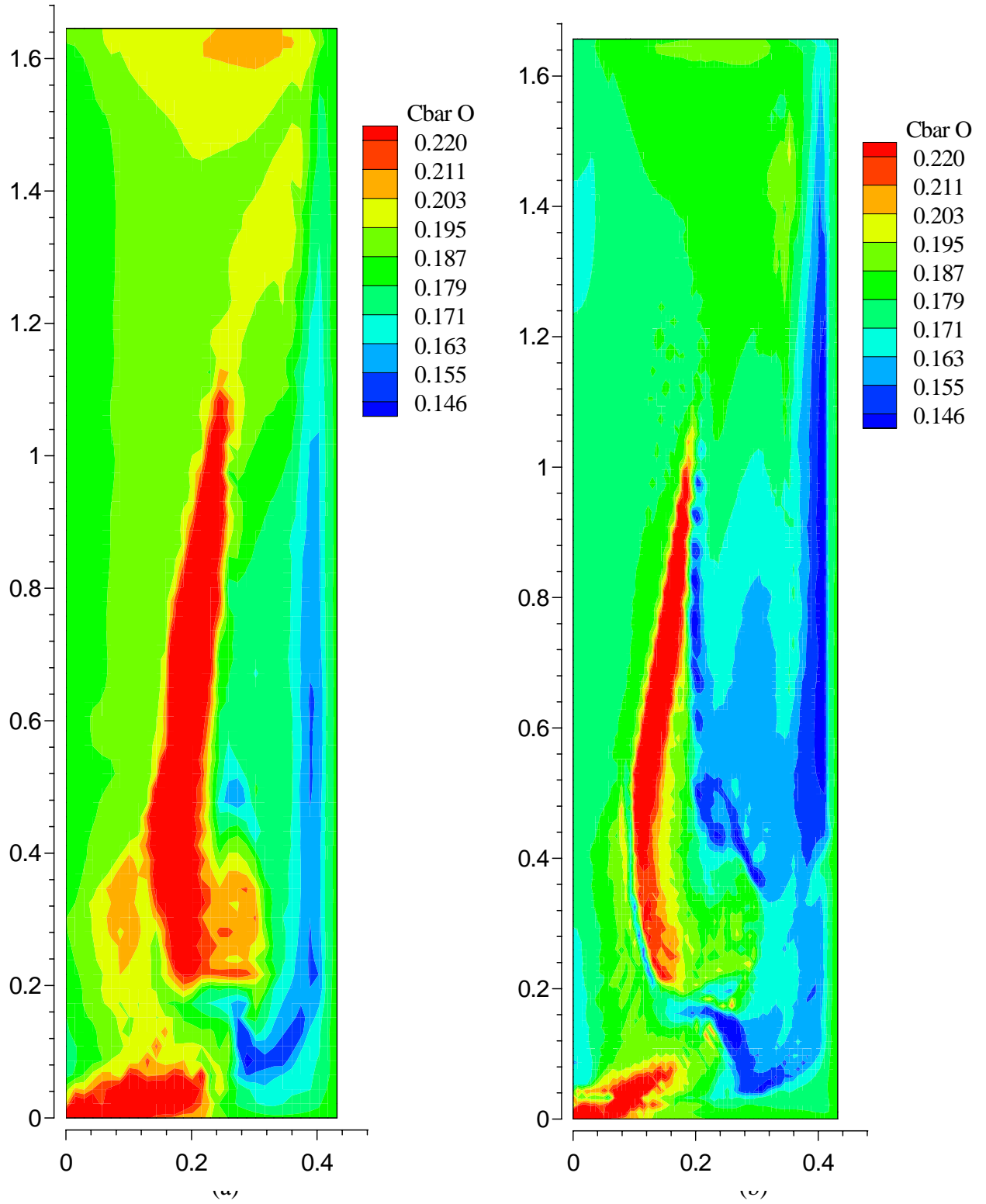
Fig. 5: Macrosegregation of oxygen calculated from MULTIA after 16000 s of ingot solidification with a primary arm spacing of 300 μm: (a) element size in mesh is 14.3 mm x 21.7 mm and (b) is 7.2 mm x 10.8 mm. Dimensions are in m.
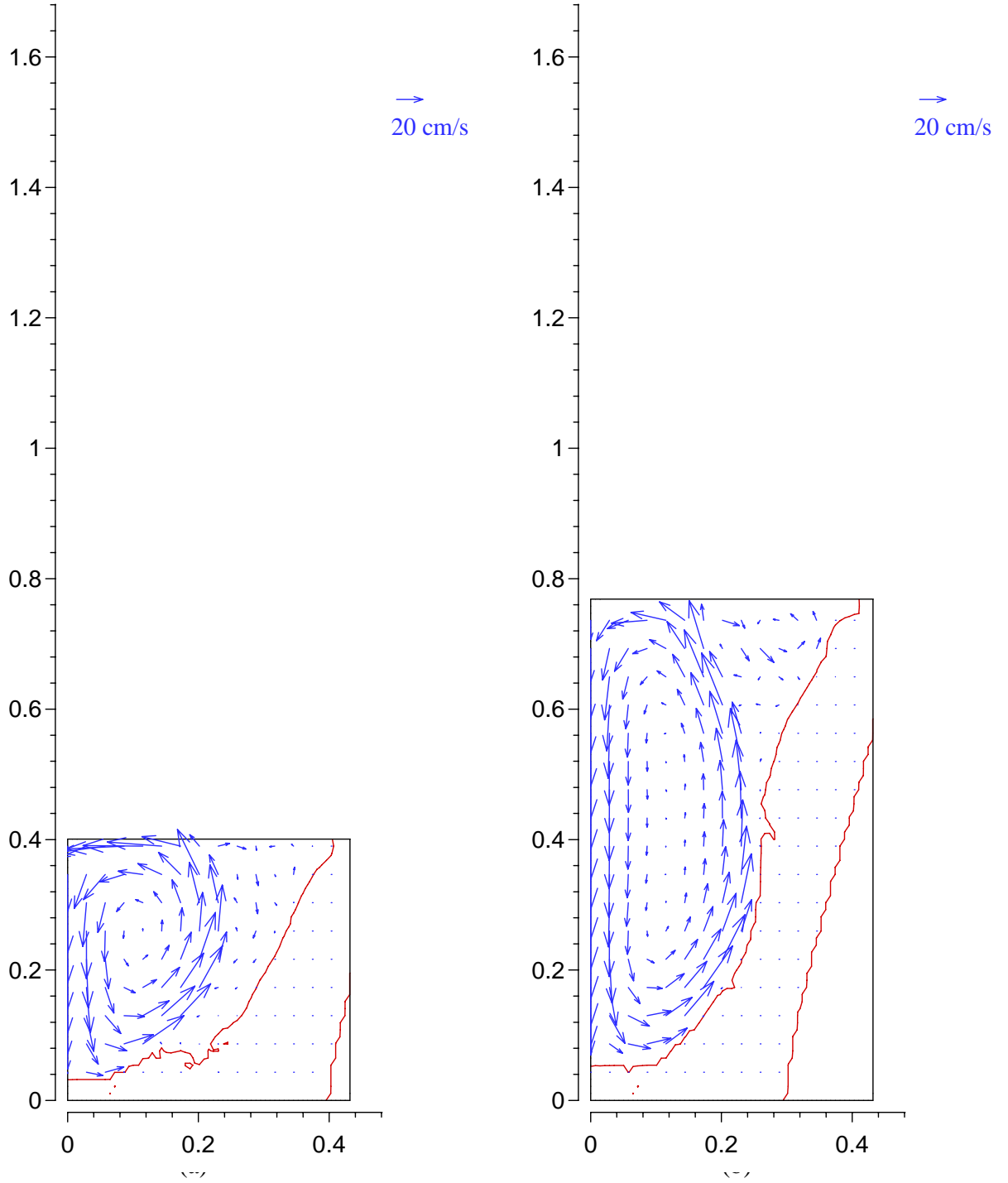
Fig. 6: Velocities calculated from MULTIA with a primary arm spacing of 300 µm and element size of 7.2 mm x 10.8 mm: (a) after 2000 s and (b) after 4000 s. The extent of the mushy zone is also shown. Dimensions are in m.

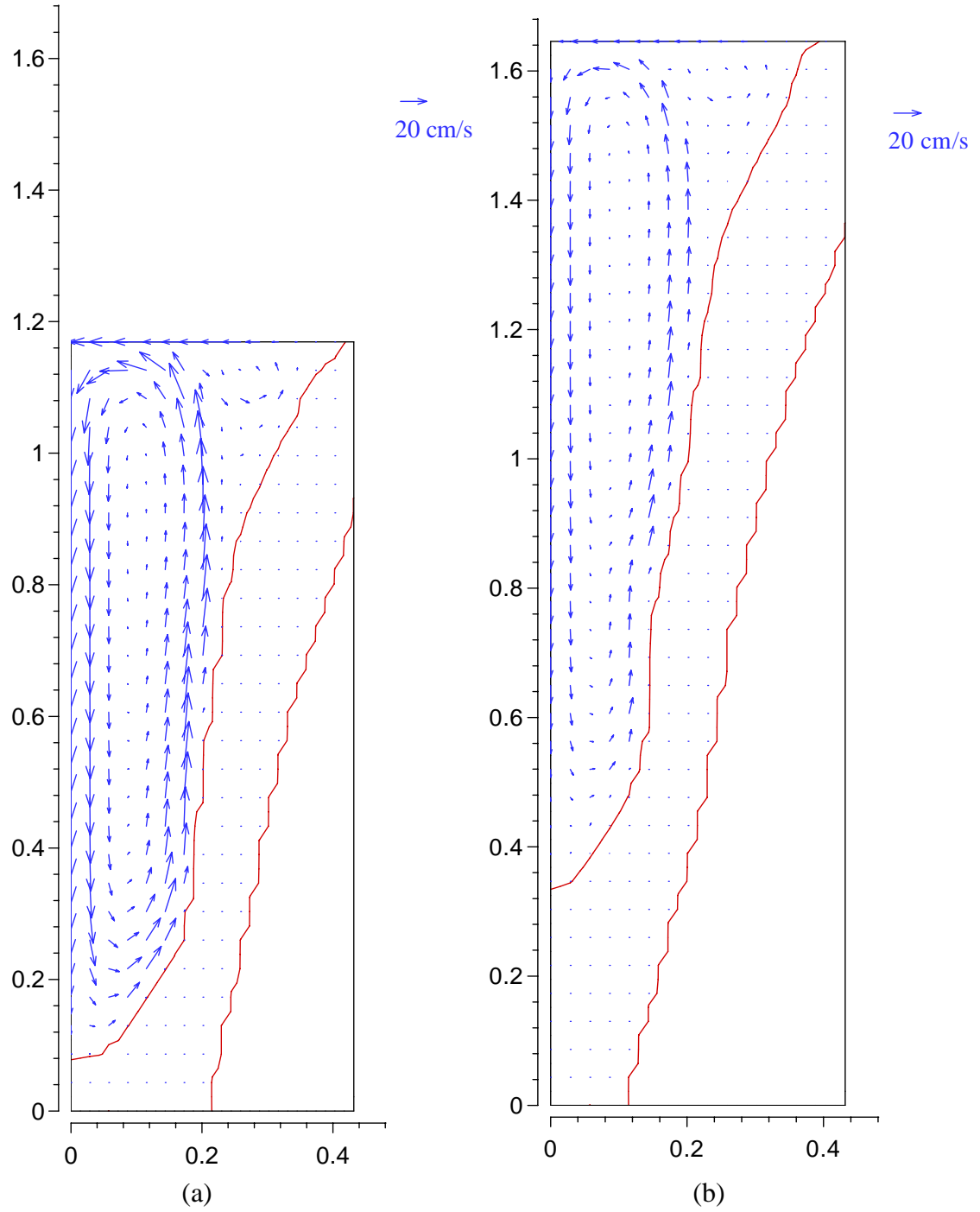Fig. 7: Velocities calculated from MULTIA with a primary arm spacing of 300 μm and elements of 7.2 mm x 10.8 mm: (a) after 6000 s and (b) after 8700 s. The extent of the mushy zone is also shown. Dimensions are in m.

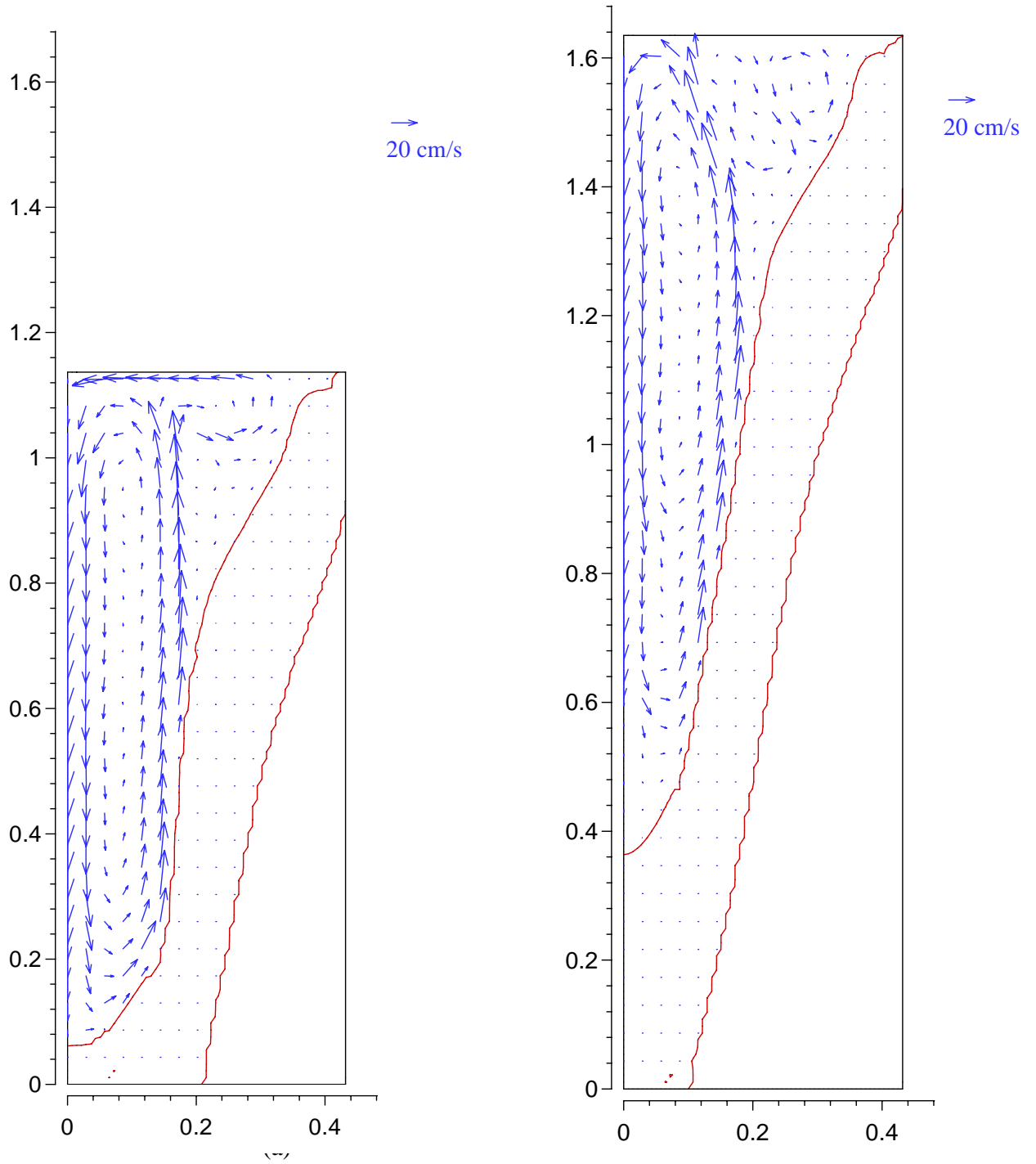Figures 4(a) and 4(b) show the macrosegregation of oxygen after 8700 s in an ingot with a primary dendrite arm spacing of 300 μm used for predicting the permeability in the mushy zone. Figure 4(a) is the result simulated with the larger mesh spacing (14.3 mm × 21.7 mm), and Fig. 4(b) is with the smaller mesh spacing (7.2 mm × 10.8 mm). Qualitatively, the segregation patterns are similar except more details of the segregation are revealed when the finer elements are used. Specifically an added band of positive segregation of oxygen exists at the mid-width of the ingot for the simulation with the finer mesh. The simulation with the larger elements shows somewhat more segregation, but the segregated bands are narrower.

Simulations of the segregation in the completely solidified ingots are given in Figs. 5(a) and 5(b). Segregations in the completely solidified ingots are similar to the results shown in Fig. 4(a) and 4(b), respectively, which indicates that the pattern of segregation was essentially developed at the earlier time. Near the right side of each ingot, there is a band depleted in oxygen and enriched in iron. In the previous section, it is reported that the vertical bands are possibly weak freckles, but the DS-set of simulation-experiments offers evidence that the Ti-6Al-4V alloy has no tendency for forming vertical freckles. Figures 6(a) and (b) and Figures 7(a) and 7(b) show the calculated velocities in the melt pool; these figures represent output after 2000 s, 4000 s, 6000 s and 8700 s of solidification of the ingot. Because of the Lorentz forces, the melt-pool sweeps upward along the leading part of the mushy zone and carries oxygen-depleted melt toward the upper right corner, where there are weak secondary convection cells. Hence, a depletion of oxygen in the right side of the ingot results, but the exact mechanism making the segregation-band near the right side of ingot is not known. Perhaps the mechanism is related to the fact that the melt pool is almost stagnant where the vertical oxygen-depleted band intersects the leading part of the mushy zone.

IV. Status of VAR-Simulations

In this report it is demonstrated that MULTIA can be used to predict the formation of macrosegregation in ingots. In its present form, however, MULTIA is an "in-house" research code without requisite "front-end" and "output" set-ups for engineering applications. There are computer codes for simulating VAR-ingots, but they are not used by USA VAR-ingot producers for predicting and controlling macrosegregation. The codes are called BAR, Calcosoft, SOLID, and COMPACT.

BAR is a proprietary code of the Specialty Metals Processing Consortium (SMPC). The industrial members are companies who produce VAR- and ESR-ingots of titanium alloys, superalloys, and specialty steels. BAR solves the energy equation, the momentum equation with a simple turbulence model, and the Lorentz forces, but does not calculate the redistribution and transport of the alloy- and impurity-elements. It does not calculate macrosegration, and it is used exclusively for VAR processing. Simulation runs using BAR are very fast, so it is a candidate for real-time control systems.

SOLID is software developed at the Laboratory of Science and Engineering of Materials and Metallurgy in the School of Mines in Nancy, France. This code can be used exclusively by companies that are contributing members to the Solidification Group at the School of Mines. SOLID simulates the solidification of ingots, including VAR-ingots, and does calculate macrosegregation. Among the SMPC members, Timet is a member company of both the School of Mines in Nancy and the SMPC and uses SOLID.

According to a user: Calcosoft is licensed by the European-based software company known as the ESI group. "CALCOSOFT-2D is a promising tool for the modeling and simulation of remelting processes like Vacuum Arc Remelting (VAR). Based on our current simulation results and on dedicated software developments in the frame of a joint project with Calcom ESI, we will be able to improve the quality of our remelted ingots by an optimization of the melt rate, the fill ratio, the cooling system and the current and voltage definitions." [Christof Sommitsch, Project Leader, Böhler Edelstahl GmbH & Co KG, Austria .] According to the Calcosoft-ESI website, a module for calculating macrosegregation is available.

COMPACT is a product of Innovative Research, Inc. (IRI). Under the COMPACT umbrella customers choose a Customized Package. SMPC included an evaluation of COMPACT for ESR-ingots as part of a year long program. The Customized Package delivered by IRI was suitable for "steady-state" ingot solidification. As of 2005 a version for analyzing ingots that solidify under transient conditions had not been released by IRI. More importantly COMPACT does not calculate macrosegregation. No USA company is using COMPACT for VAR-processing. A version of the transient VAR model is under development so that situation may change. An SMPC member believes there are three USA licensees for ESR processing.

Under the aegis of SMPC, Purdue investigators have used PHYSICA of Physica Ltd., U.K. to simulate macrosegretion in binary alloys of Ti under VAR conditions. PHYSICA is not typically used for ingot solidification, but through an arrangement that allowed the Purdue investigators access to the object code, they were able to design solidification-modules that were combined with PHYSICA to effect the simulations. The Purdue/Physica arrangement was suitable for carrying out research, but neither SMPC, Purdue nor Physica Ltd. has commercialized specialized software for VAR-ingot producers. None of the SMPC members uses PHYSICA for simulating VAR- or ESR-ingots.

As of this writing, it appears that only CALCOSOFT-2D could be used by the VAR-ingot producers in the USA for calculating macrosegregation. Timet of Henderson, Nevada is an exception because Timet is a member company of the School of Mines in Nancy, France. The members of SMPC use BAR, but of course cannot do macrosegregation calculations with it. MULTIA was originally designed to simulate the formation of macrosegregation (including freckles) in multi-component alloys that are directionally solidified. As mentioned above, in order for MULTIA to be used as an engineering tool for simulating Ti-alloy ingots there are several to many features that should be added. Appendix B summarizes enhancements to make MULTIA into an engineering tool.

Acknowledgements

References

1. S. Ganesan and D.R. Poirier: "Conservation of Mass and Momentum for the Flow of Interdendritic Liquid during Solidification," *Metall. Trans. B*, vol. 21B, 1990, pp. 173-181.

2. E. McBride, J.C. Heinrich, and D.R. Poirier: "Numerical Simulation of Incompressible Flow Driven by Density Variations during Phase Change," *Int. J. Num. Meth. Fluids*, vol. 31, 1999, pp. 787-800.

3. D.R. Poirier, P.K. Sung, and S.D. Felicelli: "A Continuum Model of Microporosity in an Aluminum Casting Alloy," *Trans. AFS*, vol. 109, 2001, pp. 379-395.

4. M.C. Flemings: *Solidification Processing*, McGraw-Hill, New York, 1974.

5. H.S. Whitesell III: *Ph.D. Dissertation*, Auburn University, Auburn, Alabama, 2002.

6. J.I. Nurminen and H.D. Brody: "Dendrite Morphology and Microsegregation in Titanium Base Alloys," in *Titanium Science and Technology*, R.I. Jaffee and H.M. Burte (eds.), Plenum Press, New York, vol. 3, 1973, pp. 1893-1914.

7. H.B. Bomberger and F.H. Froes: "Prospects for Developing Novel Titanium Alloys Using Rapid Solidification, in *Titanium, Rapid Solidification Technology*, F.H. Froes and D. Eylon (eds.), TMS, Warrendale, PA, 1986, pp. 21-43.

8. M.C. Flemings, R.V. Barone, and H.D. Brody: "Investigation of Solidification of High-Strength Steel Castings," Dept. of Metallurgy, Massachusetts Institute of Technology, Cambridge, Massachusetts. AMMRC CR 63-04/5 Interim Report, Oct. 1, 1967, for Army Materials and Mechanics Research Center, Watertown, Massachusetts.

9. A.D. Patel, R.S. Minisandram, and D.G. Evans: "Modeling of Vacuum Arc Remelting of Alloy 718 Ingots," in *Superalloys 2004*, K.A. Green (ed.), The Minerals, Metals & Materials Society, Warrendale, PA, 2004, pp. 917-924.

10. P.K. Sung, D.R. Poirier and S.D. Felicelli: "Simulating the Initiation of a Channel during Directional Solidification of a Superalloy," *Metall. Mater.Trans. A*, vol. 32A, 2001, pp. 202-207.

11. D.R. Poirier, J.C. Heinrich and S.D. Felicelli: "Simulation of Transport Phenomena in Directionally Solidified Castings," in *Proceedings of the Julian Szekely Memorial Symposium on Materials Processing*, H.Y. Sohn, J.W. Evans and D. Apelian,eds., The Minenals, Metals & Materials Society, Warrendale, PA, 1997, pp. 393-410.

12. D.R. Poirier, P.J. Nandapurkar and S. Ganesan: "The Energy and Solute Conservation Equations for Dendritic Solidification," *Metall. Trans. B*, vol. 22B, 1991, pp. 889-900.

13. S. Ganesan and D.R. Poirier: "Conservation of Mass and Momentum for the Flow of Interdendritic Liquid during Solidification," *Metall. Trans. B*, vol. 21B, 1990, pp. 173-181.

14. P.K. Sung, D.R. Poirier, and S.D. Felicelli: "Sensitivity of Mesh Spacing on Simulating Macrosegregation during Directional Solidification of a Superalloy," *Int. J. Numer. Meth. Fluids*, vol. 35, 2001, pp. 357-370.

Appendix A -Continuum Model of Dendritic Solidification

(Appendix A was prepared by D.R. Poirier, Department of Materials Science and Engineering, The University of Arizona and S.D. Felicelli, Mechanical Engineering Department, Mississippi State University.)

A.1 Introduction

This progress report details the continuum model that is the basis of the solidification simulator at The University of Arizona, which is known as MULTIA. The underlying model comprises the set of transport equations: continuity, momentum, energy and solute conservation. The mushy zone is treated as a porous medium in the model. The numerical method that is used to implement the model into MULTIA is summarized. MULTIA is a finite-element code that is used to simulate macrosegregation, especially the formation of freckles, and porosity-formation in multicomponent cast-alloys. In this report, the derivations of the conservation equations and the main features of the numerical methods and algorithms that underlie MULTIA are summarized.

A.2 Continuity Equation

The following assumptions are invoked:

(i) the solid is stationary and only the liquid convects;

(ii) the densities of the liquid and solid differ and each is constant.

Assumption (i) leads to

$$\frac{\partial}{\partial t}\left(\rho_S\, g_S + \rho_L\, g_L\right) + \nabla \cdot \rho_L\, \boldsymbol{u} \;=\; 0 \tag{A1}$$

where t is time (s); ρ_S and ρ_L are the densities of the solid and liquid (kg m^{-3})

respectively; g_S and g_L are the volume fraction of solid and liquid, respectively; and $\boldsymbol{u}$

is the superficial velocity (m s^{-1}). Equation (1) can be found in Ganesan and Poirier [A1].

In a porous medium (*i.e.*, the mushy zone) the superficial velocity is the volume flow rate

in a direction divided by the unit area perpendicular to the flow. The unit area contains

both the solid and liquid. In the liquid pool, $\boldsymbol{u}$ is simply the velocity, and in the

completely solidified part of the ingot $\boldsymbol{u} = 0$.

Since the densities of the solid and liquid are each constant, Eq. (A1) simplifies to

$$\rho_S \frac{\partial g_S}{\partial t} + \rho_L \frac{\partial g_L}{\partial t} + \rho_L \nabla \cdot \boldsymbol{u} = 0$$

but $\partial g_S / \partial t = -\partial g_L / \partial t$, so that

$$\frac{\left(\rho_L - \rho_S\right)}{\rho_L} \frac{\partial g_L}{\partial t} = -\nabla \cdot \boldsymbol{u}$$

We define the solidification shrinkage as

$$\beta = \frac{\rho_S - \rho_L}{\rho_L}$$

so the final form of the continuity equation becomes

$$\nabla \cdot \boldsymbol{u} = \beta \frac{\partial \phi}{\partial t} \tag{A2}$$

where $\phi = g_L$.

A.3 Momentum Equation

Ganesan and Poirier [A1] used the technique called volume averaging to derive the momentum equation that applies to the mushy zone, which is treated as a porous medium. The following assumptions are invoked:

(iii) the exchange of momentum because of solidification shrinkage is neglected;

(iv) the average momentum-dispersion is neglected;

(v) the Newtonian constitutive relation between stress and strain rates is assumed; and it is assumed that first order resistance to flow is adequate to describe flow (this amounts to Darcy flow).

Under these assumptions and according to Ganesan and Poirier [A1], the momentum equation is

$$\rho_L g_L \left[\frac{\partial v}{\partial t} + v \cdot \nabla v \right] = -g_L \nabla P + \rho_L g_L g + \nabla \cdot N - \mu g_L^2 [\mathbf{K}]^{-1} v \qquad (A3)$$

where v is the intrinsic velocity of the interdendritic liquid, P is the pressure (Pa), g is gravitational acceleration (m s^{-2}), μ is the viscosity of the interdendritic liquid (Pa s), $\mathbf{K}$ is the permeability tensor (m^2), and N arises from volume averaging of the deviatoric part of the stress tensor of the interdendritic liquid.

The intrinsic velocity is the volume-averaged velocity of the interdendritic liquid; it is related to the superficial velocity by

$$v = \frac{u}{\phi}$$

The fourth term on the right side of Eq. (A3) accounts for the resistance to flow offered by the dendritic network within the mushy zone. The permeability $\mathbf{K}$ is a conductivity for flow in the mushy zone, which depends on the volume fraction of liquid and a length

scale of the dendritic solid. Where $\phi = 0$ (*i.e.*, all solid), $\mathbf{K} = 0$, $\mathbf{v} = \mathbf{u} = 0$ and the

momentum equation does not apply. Where $\phi = 1$ (*i.e.*, the liquid pool), all components

of $\mathbf{K}$ are ∞, and Eq. (3) reduces to the usual Navier-Stokes equation for a liquid [A2].

Thus Eq. (A3) allows for a natural transition in momentum transport from the mushy-

zone to the liquid pool. Since ϕ is treated as an independent variable, the position of the

leading front of the mushy zone is calculated as part of the solution. Furthermore, the

liquid at the leading front of the mushy zone is not assumed to be of the nominal

composition and at the liquidus temperature of the nominal alloy.

To include the effect of shrinkage we start with the stress tensor in Eq. (A3). It

can be written as

$$\nabla \cdot \mathbf{N} \;=\; \mu \, \nabla \cdot \left[\nabla \mathbf{u} \;+\; \{\nabla \mathbf{u}\}^{\mathrm{T}} \;-\; \frac{2}{3} \{\nabla \cdot \mathbf{u}\} \mathbf{I}^{(2)} \right] \tag{A4}$$

where the second term on the right side is the transpose of the matrix $\nabla \mathbf{u}$, and $\mathbf{I}^{(2)}$ is the

second order unit tensor.

For convenience, each term in Eq. (A4) is expanded in two dimensions (x, y) with

velocity components (u, v):

$$\nabla \mathbf{u} \;=\; \begin{vmatrix} \dfrac{\partial u}{\partial x} & \dfrac{\partial v}{\partial x} \\[2ex] \dfrac{\partial u}{\partial y} & \dfrac{\partial v}{\partial y} \end{vmatrix}$$

$$\{\nabla \mathbf{u}\}^{\mathrm{T}} \;=\; \begin{vmatrix} \dfrac{\partial u}{\partial x} & \dfrac{\partial u}{\partial y} \\[2ex] \dfrac{\partial v}{\partial x} & \dfrac{\partial v}{\partial y} \end{vmatrix}$$

and

$$
\{\nabla \cdot \boldsymbol{u}\}\mathbf{I}^{(2)} \quad = \quad \begin{vmatrix} \dfrac{\partial u}{\partial x} + \dfrac{\partial v}{\partial y} & 0 \\[3ex] 0 & \dfrac{\partial u}{\partial x} + \dfrac{\partial v}{\partial y} \end{vmatrix}
$$

After summing the three matrices, we get

$$
\nabla \cdot \boldsymbol{N} \quad = \quad \mu \begin{pmatrix} \nabla^2 u \ + \ \dfrac{1}{3}\dfrac{\partial}{\partial x}(\nabla \cdot \boldsymbol{u}) \\[3ex] \nabla^2 v \ + \ \dfrac{1}{3}\dfrac{\partial}{\partial y}(\nabla \cdot \boldsymbol{u}) \end{pmatrix}
$$

or generalizing to three-dimensions:

$$
\begin{aligned}
\nabla \cdot \boldsymbol{N} \quad = \quad & \mu\left[\nabla^2 u \ + \ \frac{1}{3}\frac{\partial}{\partial x}(\nabla \cdot \boldsymbol{u})\right] && (x - \text{component}) \\[2ex]
+ \ & \mu\left[\nabla^2 v \ + \ \frac{1}{3}\frac{\partial}{\partial y}(\nabla \cdot \boldsymbol{u})\right] && (y - \text{component}) && \text{(A5)} \\[2ex]
+ \ & \mu\left[\nabla^2 w \ + \ \frac{1}{3}\frac{\partial}{\partial z}(\nabla \cdot \boldsymbol{u})\right] && (z - \text{component})
\end{aligned}
$$

where the components of $\boldsymbol{u}$ are (u, v, w). Notice that each term contains the divergence

of $\boldsymbol{u}$; continuity, Eq. (A2), is substituted so that

$$
\nabla \cdot \boldsymbol{N} \quad = \quad \mu\left[\nabla^2 u \ + \ \frac{\beta}{3}\frac{\partial}{\partial x}\frac{\partial \phi}{\partial t}\right] \ + \ \mu\left[\nabla^2 v \ + \ \frac{\beta}{3}\frac{\partial}{\partial y}\frac{\partial \phi}{\partial t}\right] \ + \ \mu\left[\nabla^2 w \ + \ \frac{\beta}{3}\frac{\partial}{\partial z}\frac{\partial \phi}{\partial t}\right]
$$

or

$$
\nabla \cdot \boldsymbol{N} \quad = \quad \mu \nabla^2 \boldsymbol{u} \ + \ \frac{\mu\beta}{3}\nabla\left(\frac{\partial \phi}{\partial t}\right) \tag{A6}
$$

Equation (A6) is substituted into Eq. (A3) to get an equation for the conservation of

momentum with shrinkage; the notation change of ϕ for g_{L} is also made and $\boldsymbol{u} = \phi\boldsymbol{v}$ is

substituted. The result is

$$\frac{\partial \boldsymbol{u}}{\partial t} + \boldsymbol{u} \cdot \nabla\left(\frac{\boldsymbol{u}}{\phi}\right) = -\frac{\phi}{\rho_{\mathrm{L}}}\nabla P + \phi\left(\frac{\rho}{\rho_{\mathrm{L}}}\right)\boldsymbol{g} + \nu\nabla^2\boldsymbol{u} + \frac{\beta\nu}{3}\nabla\left(\frac{\partial \phi}{\partial t}\right) - \nu\phi[\mathbf{K}]^{-1}\boldsymbol{u}$$

(A7)

Equation (A7) is the same as Eq. (2) in Felicelli *et al.* [A3].

The only remaining detail in the momentum equation is the Boussinesq approximation. It is assumed that the density of the liquid is constant at its reference value, ρ_{L}, in all terms except in the body force term (*i.e.*, the gravity term). For that we use

$$\frac{\rho}{\rho_{\mathrm{L}}} = 1 + \beta_T (T - T_R) + \sum_{j=1}^{N} \beta_C^j (C_{\mathrm{L}}^j - C_R^j)$$

(A8)

where

$$\beta_T \equiv \frac{1}{\rho_{\mathrm{L}}}\frac{\partial \rho}{\partial T}$$

and

$$\beta_C^j \equiv \frac{1}{\rho_{\mathrm{L}}}\frac{\partial \rho}{\partial C_{\mathrm{L}}^j} \ .$$

In Eq. (A8) N is the number of components, j refers to a component, and T_R and C_R^j refer to the reference temperature and concentration, respectively. The reference state has the coordinates:

$$T_{\mathrm{L}}, C_{\mathrm{o}}^1, C_{\mathrm{o}}^2, C_{\mathrm{o}}^3 \ldots\ldots$$

where T_{L} is the liquidus of the alloy with its nominal composition and the C_{o}'s refer to the concentrations of the elements 1, 2, 3 .... in the nominal alloy-chemistry.

A.4 Solute Conservation Equation

Assumption (i) still applies. Other assumptions at the local level are explained below. Starting with Eq. (15) from Poirier *et al.* [A4], each component in the alloy or dissolved gas-forming element follows

$$\nabla \cdot \boldsymbol{j} \; + \; \nabla \cdot (\rho_L \, C_L \, \boldsymbol{u}) \; + \; \frac{\partial}{\partial t} \left(\overline{\rho C} \right) \; = \; 0 \tag{A9}$$

(At this point, the superscript j has been omitted to simplify notation. When it is necessary to consider all of the components together, the superscript is included.) In Eq. (A9), $\boldsymbol{j}$ is the diffusion flux in kg (solute) m^{-2} s^{-1}, $\overline{\rho C}$ is the concentration in kg (solute) m^{-3}, and the second term is the advection of solute because the liquid has velocity $\boldsymbol{u}$. Equation (A9) applies to the mixture (*i.e.*, mushy zone) and the all-liquid zone. With $\boldsymbol{u} = 0$ it also applies to the all-solid zone.

For our assumptions of constant ρ_L and constant β, the advection term becomes

$$\nabla \cdot (\rho_L \, C_L \, \boldsymbol{u}) \; = \; \rho_L \, C_L \, \beta \, \frac{\partial \phi}{\partial t} \; + \; \rho_L \, \boldsymbol{u} \cdot \nabla C_L \tag{A10}$$

and by combining Eqs. (A9) and (A10), we get

$$\frac{1}{\rho_L} \nabla \cdot \boldsymbol{j} \; + \; C_L \, \beta \, \frac{\partial \phi}{\partial t} \; + \; \boldsymbol{u} \cdot \nabla C_L \; + \; \frac{\partial}{\partial t} \left(\frac{\overline{\rho C}}{\rho_L} \right) \; = \; 0 \tag{A11}$$

When Eq. (5) in Ref. [A3] is corrected, it is the same as Eq. (A11).

The mixture concentration is

$$\overline{\rho C} \; = \; \phi \, \rho_L \, C_L \; + \; (1 - \phi) \, \rho_S \, \overline{C}_S$$

or

$$\overline{C} \; = \; \phi \, C_L \; + \; (1 - \phi)(1 + \beta) \overline{C}_S \tag{A12}$$

where $\overline{C} \equiv \overline{\rho C}/\rho_L$ and $\overline{C}_S$ is the average concentration of the solute in the solid

(kg (solute) kg^{-1} or wt.%). The model considers two types of elements: those in which it is assumed there is no diffusion in the solid and those in which there is complete diffusion in the solid.

For the alloy elements with <u>no diffusion in the solid</u>, the solid that forms from the liquid is $k C_L$ with k defined as the equilibrium partition ratio. Then the average concentration of an element in the solid (wt.%) is

$$\overline{C}_S = \frac{1}{1-\phi} \int_\phi^1 k C_L d\phi \tag{A13}$$

When the model is incorporated into MULTIA, it is necessary to evaluate and store the integral at every node in the finite-element mesh.

For interstitial elements with <u>complete diffusion in the solid</u>:

$$\overline{C}_S = C_S = k C_L \tag{A14}$$

Returning to Eq. (A11), we see that the flux for diffusion in the mixture is needed. This is written as

$$\boldsymbol{j} = -\rho_L D_L' \nabla C_L - \rho_S D_S' \nabla C_S \tag{A15}$$

where D_L' and D_S' are effective diffusivities in the liquid and solid. These are

$$D_L' = \frac{\phi D_L}{\tau_L}$$

$$D_S' = \frac{(1-\phi) D_S}{\tau_S}$$

where D_L and D_S are the diffusion coefficients and τ_L and τ_S are the tortuosities to account for the morphology and connectivity of the phases. Lacking data on the tortuosities, we assume that $\tau_L = \tau_S = 1$ (Assumption vi).

For most alloy elements (*i.e.*, substitutional elements), $D_L \gg D_S$ so Eq. (A15) reduces to

$$\boldsymbol{j} = -\rho_L \phi D_L \nabla C_L \tag{A16}$$

On the other hand, some elements diffuse rapidly in the solid (*i.e.*, interstitial elements such as N, H, O and C in nickel alloys, titanium alloys, and ferrous alloys and H in aluminum alloys). These elements maintain equilibrium during partitioning; thus

$$\nabla C_S = k \nabla C_L$$

so that Eq. (A15) becomes

$$\boldsymbol{j} = -[\rho_L \phi D_L + k \rho_S (1-\phi) D_S] \nabla C_L$$

or

$$\boldsymbol{j} = -\bar{\rho} D_{mix} \nabla C_L \tag{A17}$$

Thus, the effective diffusivity of the mixture is

$$D_{mix} = \frac{1}{\bar{\rho}} [\rho_L \phi D_L + k \rho_S (1-\phi) D_S]$$

and $\bar{\rho}$ is the mixture density:

$$\bar{\rho} = \phi \rho_L + (1-\phi) \rho_S$$

Equation (A17) is the same as Eq. (11) in Ref. [A3].

A.5 Conservation of Energy

Equation (1) in Poirier *et al.* [A4] can be written as

$$\frac{\partial}{\partial t}\left(\overline{\rho H}\right) = \nabla \cdot (\kappa \, \nabla T) - \nabla \cdot (\rho_L \, H_L \, \boldsymbol{u}) \tag{A18}$$

where

$$\overline{\rho H} = \rho_S \, (1 - \phi) \, H_S + \rho_L \, \phi \, H_L \tag{A19}$$

κ is the mixture thermal conductivity, $\boldsymbol{u}$ is the superficial velocity of the liquid, and H_S and H_L are the intensive enthalpies of the solid and liquid (J kg^{-1}). The enthalpies are expressed in terms of the respective enthalpies at a reference temperature, T^H, where the heat of fusion is given. Hence

$$H_S = H_S^H + c_S \, (T - T^H) \tag{A20}$$

$$H_L = H_L^H + c_L \, (T - T^H) \tag{A21}$$

and

$$L = H_L^H + H_S^H \tag{A22}$$

where c_S and c_L are the specific heat capacities (J kg^{-1} K^{-1}) and L is the latent heat of fusion (J kg^{-1}).

The time derivative of the volumetric enthalpy in Eq. (A18) is expanded as follows:

$$\frac{\partial}{\partial t}\left(\overline{\rho H}\right) = -\rho_S \, H_S \, \frac{\partial \phi}{\partial t} + \rho_L \, H_L \, \frac{\partial \phi}{\partial t} + \rho_S \, (1 - \phi) \frac{\partial H_S}{\partial t} + \rho_L \, \phi \, \frac{\partial H_L}{\partial t}$$

$$= \left[\rho_L \, H_L - \rho_S \, H_S\right]\frac{\partial \phi}{\partial t} + \left[\rho_S \, (1 - \phi) \, c_S + \rho_L \, \phi \, c_L\right]\frac{\partial T}{\partial t} \tag{A23}$$

The advective term in Eq. (A18) is expanded while taking ρ_L = constant:

$$\nabla \cdot (\rho_L H_L \boldsymbol{u}) = \rho_L H_L \nabla \cdot \boldsymbol{u} + \boldsymbol{u} \rho_L \nabla H_L$$

$$= \rho_L H_L \beta \frac{\partial \phi}{\partial t} + \rho_L \boldsymbol{u} C_L \nabla T \tag{A24}$$

Now we combine Eqs. (A18), (A23) and (A24):

$$\left[\rho_S (1 - \phi) c_S + \rho_L \phi c_L \right] \frac{\partial T}{\partial t} = \nabla \cdot (\kappa \nabla T) - \rho_L c_L \boldsymbol{u} \cdot \nabla T - \rho_S \left[L + (c_L - c_S)(T - T^H) \right] \frac{\partial \phi}{\partial t}$$

$$\tag{A25}$$

Numerically, it is important to express the term involving $\partial \phi / \partial t$ as a function of

$\partial T / \partial t$.

The latent heat term in Eq. (A25) must be treated implicity in order for the

numerical algorithm in MULTIA to be stable [A5-A7]. To make this term implicit for a

multicomponent alloy requires that the temperature of the mixture is related to the

composition of the interdendritic liquid [A8,A9].

Consider first a solute that diffuses completely in the local solid, so that

$C_S = k C_L$ in Eq. (A12). Equation (A12) can then be written

$$\overline{C}^j = \left[K^j + (1 - K^j) \phi \right] C_L^j \tag{A26}$$

where $K^j = (1 + \beta) k^j$ and j refers to a particular element. Hence,

$$\frac{1}{K^j + (1 - K^j) \phi} \frac{\partial \overline{C}^j}{\partial t} = \frac{\partial C_L^j}{\partial t} + \frac{(1 - K^j) C_L^j}{K^j + (1 - K^j) \phi} \frac{\partial \phi}{\partial t} \tag{A27}$$

The temperature in the mushy zone is the liquidus temperature of the interdendritic

liquid, so that

$$\frac{\partial T}{\partial t} = \sum_{j=1}^{N} m^j \frac{\partial C_L^j}{\partial t} \tag{A28}$$

where $m^j \equiv dT/dC_L^j$ represents the change in the temperature as C_L^j changes and N

refers to the number of elements in the alloy.

For a reason that will become apparent, Eq. (A27) is multiplied by $\sum_{j=1}^{N} m^j$.

$$\sum_{j=1}^{N} \frac{m^j}{K^j + (1-K^j)\phi} \frac{\partial \overline{C}^j}{\partial t} = \sum_{j=1}^{N} m^j \frac{\partial C_L^j}{\partial t} + \left\{ \sum_{j=1}^{N} \frac{m^j (1-K^j) C_L^j}{K^j + (1-K^j)\phi} \right\} \frac{\partial \phi}{\partial t} \qquad \text{(A29)}$$

By Eq. (A28), the first term on the right side is simply $\partial T/\partial t$. To simplify the notation,

we define:

$$M^j \equiv \frac{m^j}{K^j + (1-K^j)\phi}$$

and

$$A_1 = (1-K^j) M^j C_L^j .$$

Finally, Eq. (A27) yields:

$$\frac{\partial \phi}{\partial t} = \frac{1}{A_1} \sum_{j=1}^{N} M^j \frac{\partial \overline{C}^j}{\partial t} - \frac{1}{A_1} \frac{\partial T}{\partial t} \qquad \text{(A30)}$$

At this point we eliminate $\partial \phi/\partial t$ in Eq. (A25) by substituting Eq. (A30); before

doing so, we divide Eq. (A25) by $\rho_L C_L$. These two steps result in

$$\left[\gamma + (1+\beta)(1-\phi) + \phi \right] \frac{\partial T}{\partial t} - \alpha \nabla^2 T = -\boldsymbol{u} \cdot \nabla T + A_2 \frac{\partial \phi}{\partial t} \qquad \text{(A31)}$$

where $\gamma = c_S/c_L$; κ is assumed to be constant; $\alpha = \kappa/\rho_L C_L$; and A_2 is defined as

$$A_2 \equiv (1+\beta) \left[(L/c_L) + (1-\gamma)(T - T^H) \right] .$$

By combining Eqs. (A30) and (A31), we obtain the energy equation without $\partial \phi/\partial t$.

$$\left[\gamma(1 + \beta)\,(1 - \phi) + \phi - A \right] \frac{\partial T}{\partial t} \;-\; \alpha\,\nabla^2 T \;\; = \;\; \boldsymbol{u} \cdot \nabla T \;-\; A \sum_{j=1}^{N} M^{\,j}\, \frac{\partial \overline{C}^{\,j}}{\partial t} \qquad \text{(A32)}$$

where $A = A_2/A_1$ in the mushy zone and $A = 0$ in the all-liquid and all-solid zones.

Recall, however, that the parameter $M^{\,j}$ (and hence A_1) depends on the assumption that

the solute elements diffuse completely in the local solid.

It remains to determine the energy equation when there is no diffusion in the local

solid. For this case we return to the equation just above Eq. (A12) and expand it as

follows:

$$\frac{\partial}{\partial t}\left(\overline{\rho C} \right) \;=\; \rho_{\mathrm{L}}\,\phi\,\frac{\partial C_{\mathrm{L}}}{\partial t} \;+\; (\rho_{\mathrm{L}} - k\,\rho_{\mathrm{s}})\,C_{\mathrm{L}}\,\frac{\partial \phi}{\partial t} \qquad \text{(A33)}$$

Equation (A33) replaces Eq. (A27) in the derivative of the final form of the energy

equation. The result is that Eq. (A32) also applies for no diffusion in the solid, but $M^{\,j}$

(and hence A_1) takes on different values:

$$M^{\,j} \;\;=\;\; \frac{m^{\,j}}{\phi} \qquad \text{(A34)}$$

Since $M^{\,j}$ is included in the definition of A_1, then it too is affected. Equation (A32) was

first presented in Ref. [A3] but without its derivation.

A.6 Numerical Method

The governing equations are solved with a finite element discretization, using

bilinear isoparametric elements, and a finite difference scheme to discretize in time. The

algorithm uses a Petrov-Galerkin formulation for stabilization of the convective terms,

and the penalty method to impose incompressibility. The algorithm solves the

conservation equations written in terms of nondimensional variables; many details are in

Refs. [A7] and [A9] and are not repeated here. However, differences in the numerical expressions and calculations procedures, arising because of the inclusion of interstitial elements and the effect of shrinkage, need to be mentioned. Also, in addition to the formal procedures involved in the finite element method, a successful numerical implementation of the solidification model requires special consideration and organization of the calculations.

A.6.1   *Computation of the Solute Concentrations in the Liquid and Solid*

The average solute concentration $\overline{C}^j$ is computed from the conservation equation, Eq. (A11). Using this value, we calculate the concentrations in the phases following the procedure described in Ref. [A9]. Some modifications need to be done, however, to allow for shrinkage and solutes that have high diffusion in the solid (like gas-forming elements). Defining

$$I^j \;=\; \int_{\phi}^{1} k^j\, C_{\mathrm{L}}^j \; d\phi \;=\; (1-\phi)\,\overline{C}_{\mathrm{S}}^j \tag{A35}$$

and proceeding as in Ref. [A9], we arrive at the following expressions for calculating the phase concentrations of solutes that have negligible diffusion in the solid:

(1) Solidification

$$I^{j,\,n+1} \;=\; I^{j,\,n} \;+\; \tfrac{1}{2}k^j\,(C_{\mathrm{L}}^{j,\,n} + C_{\mathrm{L}}^{j,\,n+1})(\phi^n - \phi^{n+1}) \tag{A36}$$

$$C_{\mathrm{L}}^{j,\,n+1} \;=\; \frac{\overline{C}^{\,j,\,n+1} - (1+\beta)[\,I^{j,\,n} + \tfrac{1}{2}k^j C_{\mathrm{L}}^{j,\,n}\,(\phi^n - \phi^{n+1})\,]}{\phi^{n+1} + \tfrac{1}{2}(1+\beta)\,k^j\,(\phi^n - \phi^{n+1})} \tag{A37}$$

(2) Remelting

$$I^{j,\,n+1} \;=\; H^j\,(\phi^{n+1}) \tag{A38}$$

$$C_L^{j,\,n+1} \;\; = \;\; \frac{\overline{C}^{\,j,\,n+1} - (1+\beta)\,I^{\,j,\,n+1}}{\phi^{n+1}} \tag{A39}$$

where the subscript n indicates the time level t^n, and H^j is a function that stores the histories of solidification for each alloy component.

For the case of solutes that have high diffusivities in the solid, the following expressions are obtained for both solidification and remelting situations:

$$I^{\,j,\,n+1} \;\; = \;\; (1 - \phi^{n+1})\,k^j\,C_L^{j,\,n+1} \tag{A40}$$

$$C_L^{j,\,n+1} \;\; = \;\; \frac{\overline{C}^{\,j,\,n+1}}{K^j + (1 - K^j)\,\phi^{n+1}} \tag{A41}$$

where $K^j = (1+\beta)\,k^j$. For simplicity of notation, the partition ratios k^j are assumed constant in Eqs. (A36) through (A41); however, the model allows them to be functions of concentration, and hence of time.

A.6.2 *Computation of the Volume Fraction of Liquid*

Here we depart from the method used in Ref. [A9], which expressed the liquidus temperature in a pseudo-lineal form and hence required that, for general nonlinear liquidus functions, modified slope coefficients $\overline{m}^{\,j}$ be calculated, in addition to the regular coefficients m^j. This is not needed in the current approach, and arbitrary liquidus functions can be easily accommodated in the model. Since the concentrations of the gas-forming elements are very small, we neglect their effects on the liquidus temperature of the alloy. The concentration of solute j in the liquid is

$$C_L^j \;\; = \;\; \frac{\overline{C}^{\,j} - (1+\beta)\,I^{\,j}}{\phi}$$

and substituting this into the liquidus function, we have

$$T_{\text{Liq}} \;=\; f(C_{\text{L}}^{\,j}) \;=\; f\!\left(\frac{\overline{C}^{\,j} - (1 + \beta)\, I^{\,j}}{\phi}\right) \;\equiv\; F(\phi)$$

The temperature is the liquidus temperature that is a function of the composition of the interdendritic liquid. Hence,

$$T \;-\; F(\phi) \;=\; 0 \tag{A42}$$

and Eq. (A42) is solved using the secant method. At time level t^{n+1} and for every node in the mushy zone, we have the following iteration scheme:

$$g^{\,i} \;=\; T \;-\; F(\phi^{\,i})$$

$$\phi^{\,i+1} \;=\; \phi^{\,i} \;-\; g^{\,i}\, \frac{\phi^{\,i} - \phi^{\,i-1}}{g^{\,i} - g^{\,i-1}}$$

For iteration $i = 0$:

$$\phi^{\,0} \;=\; \phi^{\,n}; \qquad g^{\,-1} \;=\; 0$$

where $\phi^{\,n}$ is the volume fraction of liquid at the previous time level $t^{\,n}$.

A.6.3 *Calculation of Pressure*

To obtain the velocity field, the weighted residual forms of Eqs. (A2) and (A7) (in nondimensional form) are discretized using bilinear isoparametric elements and a penalty method to impose incompressibility. The use of the penalty method, however, eliminates the pressure as an unknown, which needs to be recovered through a post-processing step. In addition, because the continuity equation (Eq. (A2)) is not homogeneous, the implementation of the penalty method differs from the standard approach used in the incompressible Navier-Stokes equations. To attack this problem, we use the method proposed by McBride *et al.* [A10]. They showed that discretizing the

continuity and momentum equations with a mixed formulation, consisting of a bilinear velocity and constant element pressure at the element level, is equivalent to the use of a penalty method with the pressure defined by the relation (in nondimensional form):

$$p = p_s - \frac{\lambda}{\text{Re}}\left(\nabla \cdot \boldsymbol{u} - \beta \frac{\partial \phi}{\partial t}\right) \tag{A43}$$

where p is the total pressure, p_s is the static pressure, $\text{Re} = VH/\nu_0$ is a Reynolds number, and λ is the penalty parameter. The penalty parameter must be a large number (e.g., $\lambda = 10^{10}$) in order to impose incompressibility effectively. This number may need to be even larger when the range of permeability in the mushy zone varies greatly, and the Darcy term becomes very large for small fractions of liquid in the mushy zone.

A.6.4 *Program Algorithm*

The governing equations are solved sequentially, and a partial iteration is performed within each time-step to obtain convergence. The iteration does not include the momentum equations, which are solved only once at the beginning of the time-step. At time t^n all conditions are known. To advance to time $t^{n+1} = t^n + \Delta t$ and whenever an equation is solved for one of the dependent variables, the latest available values for all other variables are used. The following scheme is used in the calculations:

(1) Solve for velocity and pressure, from the nondimensional momentum equation and Eq. (A43).

(2) Solve for temperature from the nondimensional energy equation.

(3) Compute fraction of liquid from Eq. (A42).

(4) Compute phase concentrations from Eqs. (A36) through (A41).

(5) Solve for mixture concentrations from the nondimensional form of Eq. (A11).

Step 1 is solved once per time level, while steps 2 through 5 are iterated within a time level until convergence. Further details on the algorithm can be found in Refs. [A7] and [A9], including treatment of remelting, solidification at the eutectic temperature, and selection of time-steps and meshing strategies.

References for Appendix A

A1. S. Ganesan and D.R. Poirier: "Conservation of Mass and Momentum for the Flow of Interdendritic Liquid during Solidification," *Metall. Trans. B*, vol. 21B, 1990, pp. 173-181.

A2. D.R. Poirier and G.H. Geiger: *Transport Phenomena in Materials Processing,* TMS, Warrendale,PA, 1994, pp. 55-56.

A3. S.D. Felicelli, D.R. Poirier and P.K. Sung: "A Model for Prediction of Pressure and Redistribution of Gas Forming Elements in Multicomponent Casting Alloys," *Metall. Mater. Trans. B*, vol. 31B, 2000, pp. 1283-1292.

A4. D.R. Poirier, P.J. Nandapurkar and S. Ganesan: "The Energy and Solute Conservation Equations for Dendritic Solidification," *Metall. Trans. B*, vol. 22B, 1991, pp. 889-900.

A5. J.C. Heinrich, S. Felicelli and D.R. Poirier: "Vertical Solidification of Dendritic Binary Alloys," *Comp. Meth. Appl. Mech. Engg.*, vol. 89, 1991, pp. 435-461.

A6. S.D. Felicelli, J.C. Heinrich and D.R. Poirier: "Simulation of Freckles during Vertical Solidification of Binary Alloys," *Metall. Trans. B*, vol. 22B, 1991, pp. 847-859.

A7. S.D. Felicelli, J.C. Heinrich and D.R. Poirier: "Numerical Model for Dendritic Solidification of Binary Alloys," *Numer. Heat Transfer, Part B*, vol. 23, 1993, pp. 461-481.

A8. S.D. Felicelli, D.R. Poirier and J.C. Heinrich: "Macrosegregation Patterns in Multicomponent Ni-Base Alloys," *J. Crystal Growth*, vol. 177, 1997, pp. 145-161.

A9. S. D. Felicelli, J.C. Heinrich and D.R. Poirier: "Finite Element Analysis of Directional Solidification of Multicomponent Alloys," *Int. J. Num. Meth. Fluids*, Vol. 27, 1998, pp. 207-227.

A10. E. McBride, J.C. Heinrich, and D.R. Poirier: "Numerical Simulation of Incompressible Flow Driven by Density Variations during Phase Change," *Int. J. Num. Meth. Fluids*, vol. 31, 1999, pp. 787-800.

A11. P.K. Sung, D.R. Poirier, S.D. Felicelli, E.J. Poirier and A. Ahmed: "Simulations of Microporosity in IN718 Equiaxed Investment Castings," *J. Crys. Growth*, vol. 226, 2001, pp. 363-377.

A12. D.R. Poirier, P.K. Sung and S.D. Felicelli: "A Continuum Model of Microporosity in an Aluminum Casting Alloy," *Trans. AFS ,* vol. 109, 2001, pp. 379-395.

A13. P.K. Sung, D.R. Poirier and S.D. Felicelli: "Predicting Microporosity in Steel Castings," *Modelling Simul. Mater. Sci. Eng.,* vol. 10, 2002, pp. 551-568.

Appendix B - Enhancements to MULTIA for Simulating Macrosegregation in VAR-Ingots

1. *Building an Ingot.* In the course of this program, the capability of adding material to the calculation domains the ingot is formed from the consumable electrode was implemented

2. *Cylindrical Coordinates.* In this program, the MULTIA demonstrations were for an ingot shaped as a slab. Rectangular coordinates were used. For VAR applications, however, cylindrical coordinates are applicable. MULTIA can be run with cylindrical coordinates, but the matrices are ill-conditioned and the execution time is excessive. There are better techniques for solving the matrices that result when cylindrical coordinates are used, and these should be pursued.

3. *Motion of Equiaxed Grains.* Presently MULTIA assumes that the solid in the mushy zone is stationary. The solidifying equiaxed grains in VAR-ingots, however, are free to convect with the liquid until the fraction of solid achieves a critical concentration, above which the grains develop a stationary network of the dendritic grains. The motion of the solid can contribute to the overall segregation, so incorporating this into MULTIA would improve macrosegregation predictions.

4. *Lorentz Forces.* In this program, the Lorentz forces were transferred from BAR and added as body forces in MULTIA. It would be relatively easy to incorporate the electro-magnetics to make MULTIA independent in this regard, once correct boundary conditions for current distribution are established.

5. *Thermal Boundary Conditions.* In this program, the boundary temperatures were transferred from BAR to MULTIA. Boundary conditions in the VAR-process are complex and should be thoroughly assessed. The major complexities include heat transfer coefficients that vary with time and location as a gap develops, inclusion of the bottom stool (starting block) in the calculation-domain, energy- and material-transfer from the consumable electrode, proper boundary conditions to capture radiation exchange among the melt-surface, electrode and crucible wall, etc.

6. *Conformable Meshing.* A major restriction is that the mesh should be refined enough so that between the liquidus and the solidus of the mushy zone there are several elements (say 5 to 10) at a given elevation in the ingot. The mushy zones in Ti-ingots are rather thin which means that in a uniform mesh the total number of elements in the computational domain can be very large. Hence, conformable meshing to accommodate small elements in the mushy zone and larger elements in the liquid pool and solidified portion of the ingot should be adapted to MULTIA to keep computational times within reason.

7. *Turbulence.* MULTIA assumes laminar flow in the liquid pool. Turbulence models should be assessed: the one presently in BAR with "eddy" transport properties; simple estimates of mixing lengths for Reynolds' stresses; the often applied "k-ε" model, which

is used in many commercial codes; and a "large eddy" model. These are listed in order of sophistication and computational time!). The last in the list has been used to simulate melt flows (forced convection) in continuous casting of steel. In VAR-pools, however, flows are driven by body forces (sum of the buoyancy- and Lorentz-forces).

8. *Parallelization.* Even in its present form, MULTIA runs for tens of hours to make a simulation. With the enhancements outlined herein, it is expected that computational times would increase. Hence, MULTIA should be set up for multi-processor systems.

Appendix C - Formation of Microporosity in Thin Wall Investment Castings of IN718

A series of Progress Reports on porosity in experimental plate-castings of IN718, along with details of a solidification model, were submitted. The contract support from AFML was supplemented with an unrestricted grant from Honeywell Engines in Phoenix, AZ. The progress reports are listed in Table C1, and the major findings are summarized.

Table C1. Progress Reports under Award F33615-02-1-5219, "Formation of Micro-porosity in Thin Wall Investment Castings of IN718."

Date of Report	UA Authors	Subject(s)
09/13/2003	Poirier and Sung	Solidification model and simulations
11/02/2003	Lyman and Poirier	Fluorescent penetrant (FPI) and radiography
01/09/2004	Lyman and Poirier	Porosity assessment via quantitative metallography
02/25/2004	Lyman and Poirier	Comparison of FPI and quantitative metallography
04/12/2004	Lyman, Sung and Poirier	Distribution of porosity
06/25/2004	Lyman, Sung and Poirier	Grain size, arm spacings and porosity

Experimental castings of IN718 were made by investment casting under vacuum at two Howmet Casting facilities: the Howmet Research Center in Whitehall, Michigan and a foundry in LaPorte, Indiana. In Whitehall experimental plates of thickness 0.04, 0.08 and 0.12 inches were cast horizontally. The set of castings made in LaPorte was designed by Honeywell Engines as part of an in-house program on assessing the efficacy of thin wall castings. In LaPorte, the experimental plates of thickness 0.04 and 0.055 inches were cast vertically. Other variables included the use of a grain-nucleating agent in the face-coat of the shell mold and superheat. Some of the molds made in the LaPorte foundry were bottom-filled and some were top-filled.

Computer simulations at The University of Arizona revealed that castings with larger grain sizes had less porosity. Permeability for the flow of shrinkage metal through the mushy zone is higher for larger grains. Hence, pressure within the mushy zone is greater than in a mushy zone in a casting with fine grains. The greater the pressure in the

mushy zone, the less likely porosity develops. Superheat and mold preheat, according to the simulations, enhanced progressive solidification, resulting in somewhat less porosity. Nitrogen content was not an important variable.

The horizontally oriented plates cast in the Whitehall facility had extensive indications of porosity as picked up by fluorescent dye penetrant inspection (FPI). The "non-nucleated" plates had less porosity-indications than did the "nucleated" ones, and the least amount of porosity was found at the intermediate thickness. The porosity in the same plates was also analyzed using quantitative metallography. Plates cast in molds with a nucleating agent, exhibited porosity of less than 0.05 vol. % to about 0.2 vol. %. With the use of a nucleating agent in the mold-face coat, the porosity was greater. The worst cases had 0.2 to 0.45 vol. %. In some cases the porosity was not uniformly distributed, with as much as 10 vol. % measured near the surface. A weak positive correlation ($R^2 =$ 0.5) was observed between quality assessments made by FPI and by the quantitative metallography.

The experimental castings made at the LaPorte foundry also exhibited porosity, but the porosity was almost entirely internal. Unlike the castings made in Whitehall, the porosity was not surface-connected. In terms of incidental near-surface porosity (not surface-connected), castings in the top-filled molds displayed significantly higher amounts than the castings made in bottom-filled molds. Presumably, with bottom-filling there is significantly less turbulence and splashing of the melt as it fills the mold cavity, which results in less nonmetallic inclusions that nucleate pores. The incidental near-surface porosity was associated with the high concentrations of internal porosity, particularly in the thinner plates.

In addition to assessing the porosity, grain sizes and secondary dendrite arm spacings (SDAS) were measured. The plates cast at the Whitehall facility had average grain sizes that ranged from 0.1 mm to 9 mm. Castings made in a mold with a nucleating face-coat were markedly smaller that those made in a mold without the nucleating face-coat. Even with the nucleating face-coat, however, some of the thickest plates (0.120 in.) contained relatively large grain sizes of greater than 1 mm. The average SDAS of the castings varied between 22 and 37 μm, depending on the thickness of the plate.

The set of castings made in the LaPorte facility comprised castings in two top-filled molds and two bottom-filled molds; the former had an inoculating face-coat, while the latter had no face-coat. With a nucleating face-coat, the average grain size ranged from approximately 1 mm, near the ingate, to 0.05 mm, near the extremity of the casting. The average grain sizes in the castings made without the nucleating agent in the mold, varied between 0.75 and 1.2 mm along the length of the casting. In the overall population, the finer grains (< 0.5 mm) were columnar and met at the centerline. The larger grains (> 0.5 mm) were more randomly oriented and equiaxed. The average SDAS in the castings made in the LaPorte foundry ranged 21.4 μm to 25.1 μm. Small pores were distributed throughout the thickness of the castings, while the larger and more complex-shaped pores dominated the centerlines. The larger and more complex pores, at the centerlines, formed between grains.

Perhaps the most significant finding was the extensive surface-connected porosity found in the castings made in Whitehall, while there was hardly any or none found in the castings made in LaPorte. This suggests that the period between when a mold is filled and when the chamber vacuum is broken differed in the two facilities. More importantly, a

systematic study of the formation of surface-connected porosity should be effected, so that controlling processing conditions to mitigate its formation can be ascertained. Internal porosity is tolerable because for critical applications subsequent hot-isostatic pressing (i.e., hipping) is part of the production cycle. Hipping, however, does not eliminate surface-connected porosity.